

A dynamic view of proton-coupled electron transfer in photocatalytic water splitting

Adriano Monti, Jessica M. de Ruiter, Huub J. M. de Groot, Francesco Buda*

Leiden University, Leiden Institute of Chemistry, Einsteinweg 55, 2300 RA, Leiden, The Netherlands

ABSTRACT

Solar-driven water splitting is a key reaction step in a photoelectrochemical cell for solar fuel production. We propose a photoanode in which a TiO_2 substrate is functionalized with a supramolecular complex consisting of a fully organic naphthalene-diimide (NDI) dye covalently bound to a mononuclear Ru-based water oxidation catalyst. By performing ab-initio Molecular Dynamics simulations we elucidate microscopic details of water oxidation at the photoanode induced by visible light absorption. The fast photoinduced electron injection from the NDI into the semiconductor provides the driving force for the activation of the Ru catalyst. The proton-coupled electron transfer nature of this catalytic reaction path is unveiled through the explicit description of the water environment, which is essential to determine the proton diffusion channel and the free energy change along the reaction. The mechanistic insight into the photocatalytic processes obtained with our computational strategy can facilitate the design of new and efficient photoelectrochemical devices.

INTRODUCTION

Direct conversion of solar energy into storable chemical fuel is a promising strategy on the path towards sustainable energy sources^{1,2}. Natural systems perform this task by converting water molecules into O₂ and high-energy-density molecular compounds.^{3,4} They apply molecular machineries, which are complex, but without redundancy in the biological context of the membrane and the cell. The design of artificial solar energy conversion devices⁵ aims at applying essential fundamental principles governing natural photosynthesis, while aiming for dedicated solar to fuel conversions, which allows using a much simpler structure.⁶⁻¹²

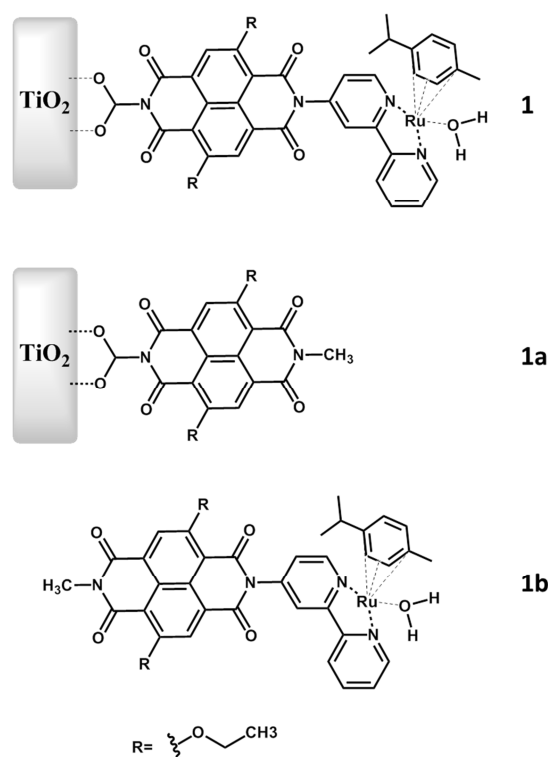
A photoelectrochemical solar fuel cell device combines the functions of light harvesting, charge separation and catalysis.¹³⁻¹⁵ In the last decade several systems have been proposed employing either metal oxide nanoparticles^{8,16-24} or molecular complexes^{8,25-28} as water oxidation catalyst (WOC). Furthermore, the coupling between the WOC, the chromophore and an electron accepting semiconductor into a photoanode has been achieved through co-absorption of both the catalyst and the chromophore^{16,29-32} or through dye-WOC supramolecular complexes.³³⁻³⁶

Acquiring a fundamental understanding of the electron transfer processes and catalytic water oxidation mechanism following light excitation of the photoanode is essential for the design and the optimization of solar fuel cells. However, this is a challenging task mainly because of the different time scales of the processes occurring upon photoexcitation. In this work we introduce a computational strategy to tackle this problem by bridging the description of the electron injection and catalytic water oxidation mechanisms. This approach is applied to photoanode **1** (see **Scheme 1**), representing a computational design option for visible light water splitting.

In system **1** a Ru-based WOC is covalently bound to an organic chromophore that is directly anchored to a TiO₂ semiconductor surface. TiO₂ is by far the most common choice for the semiconductor to be used in a dye-sensitized photoelectrochemical cell (DS-PEC)⁸, due to its excellent stability in combination with a high density of states of its conduction band, which allows for rapid electron injection rates³⁷⁻³⁹. The WOC considered in this system is the mono Ru-complex [(cy)Ru^{II}bpy(H₂O)]²⁺. This catalyst has been already theoretically and experimentally investigated in the literature, and its catalytic cycle has been suggested to proceed through four consecutive proton-coupled electron transfer (PCET) steps^{40,41}.

The molecular chromophore 2,6-diethoxy-1,4,5,8-diimidenaphthalene (NDI₁) has been already employed as visible light antenna for solar energy conversion applications.^{42,43} The family of NDI chromophores has found wide applications in dye-sensitized devices since their optical properties can be easily tuned over a wide light-spectrum.⁴⁴

Furthermore, they allow the construction of n/p-supramolecular heterojunctions presenting antiparallel gradients in electron and holes channels to achieve photoinduced long-distance charge separation and reduce charge recombination.^{45–48}



Scheme 1. Schematic representation of the proposed photoanode (**1**) including the acceptor-semiconductor (TiO₂), the molecular chromophore NDI₁, and the Ru-based water oxidation catalyst; (**1a**) chromophore-semiconductor subsystem employed for the photoinduced electron injection simulation; (**1b**) chromophore-catalyst subsystem used in the simulation of the first water oxidation catalytic step. R represents the diethoxy moiety functionalizing the chromophore naphthalene core.

The chosen NDI₁ antenna absorbs at wavelengths of ~ 470 nm and is characterized by ground and excited states oxidation potentials of ~ -6.16 eV⁴³ (vs. vacuum) and ~ -3.8 eV⁴³ (vs. vacuum), respectively, which provide a good match with the semiconductor band edge and the catalyst oxidation potential of ~ -6.2 eV vs. vacuum.⁴¹ These properties allow the NDI₁ to undergo photoinduced electron injection into the TiO₂ conduction band (~ -4 eV vs. vacuum) with little energy loss. At the same time, due to its ground state oxidation potential, the NDI₁ photoexcitation is able to trigger the catalytic activity of the [(cy)Ru^{II}bpy(H₂O)]²⁺ WOC.⁴¹

We show that the photoexcitation of system **1** induces the heterogeneous electron injection and the first PCET step for catalytic water oxidation. These two strongly correlated processes are found to proceed on different time scales. The ultrafast nature of the electron injection between NDI₁ and TiO₂ in system **1a** (**Scheme 1**) is found

through nonadiabatic dynamics. On the other hand the dynamical description of the first catalytic water splitting step is obtained with adiabatic *ab initio* constrained MD simulations performed for the oxidized antenna-catalyst model **1b** (**Scheme 1**). The use of an explicit solvent highlights the active role of the water environment in defining the water oxidation reaction path^{49–52} and its PCET character. The free energy barrier and the thermodynamic driving force are characterized along the reaction path. The computational strategy applied in this work represents an invaluable tool to describe a wide range of photo-catalytic reactions and can provide guidelines for the development of solar energy conversion devices.

COMPUTATIONAL DETAILS

Quantum-classical simulation of model 1a. The chromophore of model **1a** is prepared by functionalizing the NDI₁ molecule with a carboxylic acid anchoring group on one of the amide moieties. The geometry of the chromophore is then optimized in vacuum with the ADF software package^{53,54} at the density functional theory (DFT) level employing the exchange-correlation functional OPBE⁵⁵ and the TZP Slater type basis set.

The optimized chromophore is attached to the TiO₂ surface through the carboxylate bridge in a bidentate anchoring mode to form model **1a** shown in **Scheme 1**.

The electronic properties of this model are described by means of a tight-binding Hamiltonian based on the extended Hückel (EH) theory^{56,57}. For the optimization of the NDI₁ atomic parameters, the experimental ground-state (-6.16 eV vs. vacuum) and excited state (-3.82 eV vs. vacuum) redox potentials⁴³ are taken as target values for the HOMO and LUMO energies of the chromophore. For the atoms of the semiconductor slab, standard EH parameters⁵⁸ are employed without any further modification. An exhaustive description of the parameterization procedure can be found elsewhere^{59,60}.

The time evolution of the electronic wavepacket is performed through the atomic orbitals/molecular orbitals (AO/MO) time-propagation method⁶¹ described in the Supporting Information and in **Scheme SI1**. This methodology has been already applied successfully for the description of nonadiabatic heterogeneous electron transfer processes^{62,63}. In this method the wavepacket is evolved under the influence of an underlying nuclear trajectory⁶⁴. This ground state nuclear trajectory is calculated for model **1a** through *ab initio* Molecular Dynamics using the Car-Parrinello MD (CPMD) code⁶⁵. The MD simulations are performed in vacuum using the pseudopotentials of references^{66,67} with a plane wave cut-off of 70 Rydberg and the OPBE⁵⁵ exchange correlation functional. Applying the Nosé-Hoover thermostat, the whole **1a** model is brought to a temperature of 300 K and allowed to equilibrate for ~2 ps using a time step

of $\delta t = 0.1$ fs. The second half of this nuclear trajectory is used for the electronic wavepacket propagation, which is carried out using the same time step of the CPMD simulation.

To model the TiO_2 surface, an orthorhombic supercell with lattice parameters $a=10.239$ Å, $b=15.137$ Å and $c=40$ Å is used, together with periodic boundary conditions. The cell contains a two layers anatase slab $(\text{TiO}_2)_{32}$ functionalized with the NDI_1 chromophore.

DFT electronic and optical characterization of model **1b**

Using the ADF software package, the ground state geometry of system **1b** is initially optimized at the DFT level using the OPBE exchange-correlation functional⁵⁵ and the TZP basis set. The optimization is performed in an aqueous environment simulated with the continuous solvation model (COSMO^{68,69}) implemented in ADF.

The OPBE exchange-correlation functional has been shown to provide accurate descriptions of transition metals complexes⁷⁰⁻⁷², among which the $[(\text{cy})\text{Ru}^{\text{II}}\text{bpy}(\text{H}_2\text{O})]^{2+}$ catalyst⁴⁰ used in system **1b**. In particular, the oxidation potential of the $[(\text{cy})\text{Ru}^{\text{II}}\text{bpy}(\text{H}_2\text{O})]^{2+}$ catalyst computed with OPBE is found to be -6.2 eV, in good agreement with the experimental data.⁴¹ The same computational setting closely reproduces the experimental ground state oxidation potential for NDI_1 (-6.16 eV)⁴³ within the **1b** complex, giving a value of -6.05 eV vs. vacuum calculated using the ΔSCF approach.

TD-DFT calculations for the absorption spectrum of system **1b** are performed using the ADF software package at the B3LYP⁷³/TZP level of theory. The aqueous solution is described within the COSMO model. The choice of the exchange correlation functional is justified by the results presented in reference⁴², where B3LYP has been shown to accurately reproduce the experimental optical properties of the NDI_1 molecule.

Constrained *ab initio* MD of model **1b**

To investigate whether the photoinduced oxidation of the dyad can initiate the catalytic process of water oxidation, *ab initio* MD simulations are performed for the singly oxidized form of the catalyst-antenna complex **1b**⁺ with the CPMD program. To obtain a realistic description of the PCET reaction, the solvent is explicitly introduced in the simulation^{40,51,74}. An orthorhombic box of dimensions $25 \times 17.6 \times 14.5$ Å³ is used, containing the **1b** solute and 162 water molecules. Both the solvent and the solute molecules are treated at the same quantum-mechanical level employing the OPBE exchange correlation functional and the dispersion-corrected atom-centered pseudopotential of reference⁶⁶. Periodic boundary conditions are applied together with a plane wave cut-off of 70 Rydberg. The time step in the *ab initio* MD simulations is $\delta t = 0.1$ fs. The solvated system has been equilibrated with the following procedure:

First the water solvent is equilibrated at room temperature for about 1 ns using the TIP3P model implemented in the CHARMM force field, while the WOC-dye molecular complex is kept fixed. Then the whole system, including the complex **1b** in the non-oxidized state, is further evolved for about 100 fs using the CPMD code. Finally, one electron is removed from the simulation box and the oxidized state is evolved for ~3 ps at room temperature by applying the Nosé-Hoover thermostat.

To sample regions of the phase space that would be rarely visited during a standard MD simulation, such as transition states, a rare event simulation technique is required. Specifically, we apply the so called Blue-Moon approach, consisting in forcing the system to explore the region of interest by constraining a given reaction coordinate during the MD simulations⁷⁵⁻⁷⁷. The distance between one of the protons of the water molecule coordinated to the Ru atom, and the oxygen of one of the adjacent solvating water molecules is chosen as the constrained reaction coordinate. Five points within the range 1.4-0.98 Å are considered for this coordinate. For every value of the constraint, the system is evolved until the associated average Lagrange multiplier, corresponding to the gradient of the free energy associated to the reaction coordinate, is equilibrated.⁷⁷ The free energy variation for the whole process is then obtained via thermodynamic integration.

RESULTS AND DISCUSSION

The results are organized as follows: first, the optical properties of the [(cy)Ru^{II}bpy(H₂O)]²⁺-NDI₁ dyad **1b** are presented. The study of the photoinduced electron injection for model **1a** is presented in the next section. Finally, the mechanism of the first water oxidation step is investigated using model **1b**.

TD-DFT characterization of the electronic excitations of the dye-catalyst complex and Molecular Orbitals localization

In order to evaluate the optical properties of the NDI₁ antenna coupled to the water oxidation catalyst [(cy)Ru^{II}bpy(H₂O)]²⁺, a time-dependent DFT calculation is performed for the dyad **1b** in a water environment described through a continuous solvation model.

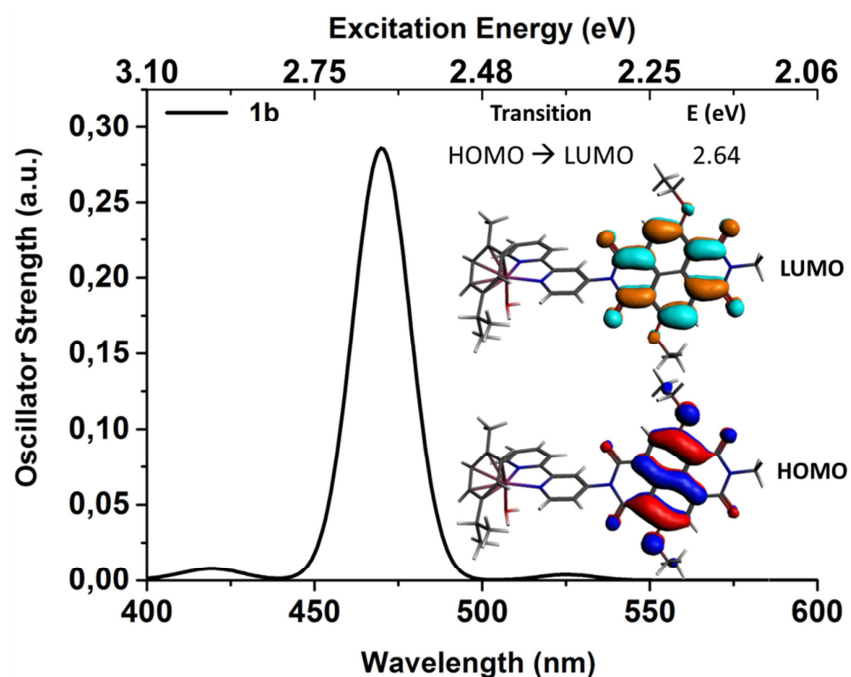


Figure 1. Optical absorption spectrum of system **1b**, computed at the B3LYP/TZP level of theory. The water solvent is included through the continuum solvation model (COSMO) as implemented in the ADF software package⁵³. The oscillator strength is in arbitrary units (a.u.). The inset shows the localization of the HOMO and LUMO, which are the only orbitals involved in the optical transition at 2.64 eV.

The results in **Figure 1** show the presence of a single dominant peak within the visible light spectral range at ~470 nm. The analysis of this electronic excitation reveals that it is associated with the HOMO to LUMO transition, localized on the chromophore subunit (see inset **Figure 1**).

The calculated optical absorption energy compares well with the experimental data and computational results for the monomer NDI₁ reported in references ⁴⁴ and ⁵⁹. This result provides evidence that the visible-light photoexcitation of the dyad does not involve the Ru-catalyst subunit, which consequently is not expected to play a significant role in the formation of the sensitizer excitonic state. This justifies investigating the process of photoinduced electron injection into the semiconductor without explicitly including the catalyst in the definition of the electron donor (see model **1a**).

Photoinduced electron injection dynamics in the NDI₁-TiO₂ model **1a**

The photoinduced electron injection dynamics is performed using the tight-binding extended Hückel approach. The computed density of states (DOS) for model **1a** obtained with the optimized Hückel parameters (see **Figure S11** in the Supporting Information) shows that the LUMO energy of the chromophore falls near the conduction band edge of TiO₂. This feature of the electronic structure of model **1a** should allow for photoinduced electron injection while limiting to a minimum the loss of the potential induced by the

photoexcitation in the form of heat.

Based on the TD-DFT results, the instantaneous photoexcitation of NDI₁ is simulated by promoting an electron from the HOMO to the LUMO of the chromophore. This initial wavepacket state is reported in **Figure 2** (inset (a)).

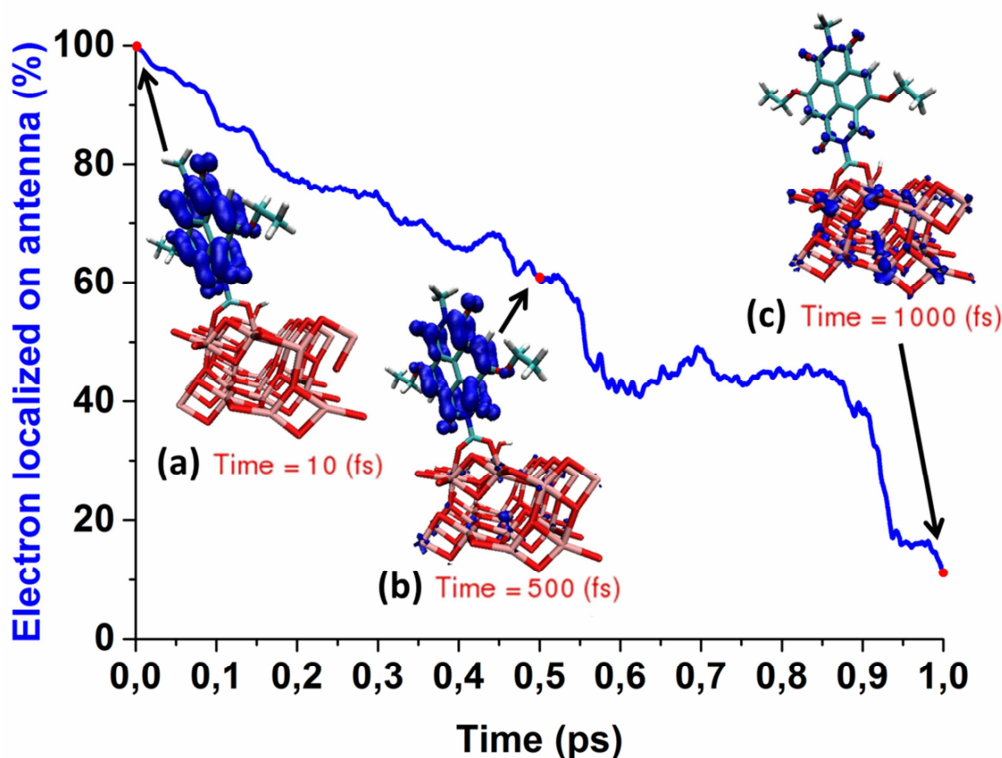


Figure 2. Electron injection profile obtained through the time-dependent population analysis of the wavepacket projected only over the NDI₁ antenna (blue line). The insets show the distribution of the total wavepacket after initialization (a), and along the MD trajectory (b and c).

The results of the electron quantum dynamics coupled to the nuclear motion show that the electron injection occurs in about 1 ps. Inset (c) in **Figure 2**, shows that at the end of the simulation the wavepacket is almost completely localized at the TiO₂ surface. Overall, these results provide clear converging evidence that system **1** can undergo electron injection upon photoexcitation of its NDI₁ antenna unit.

In general, water oxidation catalysis is known to occur over time scales orders of magnitude larger than the picosecond electron injection process observed here for system **1a**^{4,78,79}. Therefore, it is reasonable to assume that, upon photoexcitation, the electron injection will occur before the catalytic water oxidation can take place, leaving the antenna-catalyst dyad in an oxidized state.

An open issue in the context of dye-sensitized devices is the need to slow down the charge recombination process from the semiconductor into the oxidized sensitizer, since this quenching process can severely limit the quantum yield of the DS-PEC device. The quantum dynamics for the electron injection has been then extended for a further

picosecond during which no sign of electron recombination has been observed, indicating a stable charge separated state on this time scale. The potential problem of charge recombination can be also alleviated by inserting appropriate molecular bridge units with rectifying properties between the dye and the semiconductor^{16,59,80,81} or by engineering n/p-supramolecular heterojunctions.⁴⁵⁻⁴⁸ We will no further address this point in this work and assume a long-lived oxidized state.

In the next section, it is shown that this oxidized state of the antenna-catalyst dyad (**1b**) is able to drive the first catalytic step of water oxidation.

First PCET catalytic water oxidation step

Ab initio molecular dynamics simulations are performed for the oxidized dyad model **1b** in an explicit water solvent. Since we are interested in describing the proton-coupled electron transfer step, it is essential to treat the water molecules at the same DFT quantum-mechanical level of the solute. Proton diffusion in liquid water is a complex process that involves covalent bond breaking and formation within the hydrogen bonding network⁸²⁻⁸⁶. This process is commonly described within the framework of the Grotthuss mechanism⁸⁷.

After equilibration of the dyad in its initial stable intermediate $[(\text{cy})\text{Ru}^{\text{II}}\text{bpy}(\text{H}_2\text{O})]^{2+}\text{-NDI}_1$, the instantaneous photoexcitation and ultrafast electron injection are mimicked by removing an electron from the simulation box, creating the oxidized intermediate $[(\text{cy})\text{Ru}^{\text{II}}\text{bpy}(\text{H}_2\text{O})]^{2+}\text{-NDI}_1^+$. Therefore, we can monitor the localization of the photoinduced hole along the *ab initio* MD simulation by tracing the spin density of the unpaired electron. It is observed that at the beginning of the simulation ($t=0$) the hole is localized on the NDI_1 .

The oxidized system is then equilibrated at room temperature for about 3 ps (see **Figure 3**). The analysis of this MD trajectory shows that the water molecule w1, coordinated to the Ru center, forms strong hydrogen bonds with nearby solvent molecules. In **Figure 3**, the $\text{H}(\text{w1})\text{-O}(\text{w1})$ (black line) and the $\text{H}(\text{w1})\cdots\text{O}(\text{w2})$ (blue line) distances along the MD trajectory are reported. Spontaneous attempts of proton transfer from w1 to the neighbor water molecule w2 (see inset in **Figure 3**) are observed after about 1.6 ps and 1.9 ps, when the $\text{H}(\text{w1})\text{-O}(\text{w1})$ and $\text{H}(\text{w1})\cdots\text{O}(\text{w2})$ distances are almost equal. During these attempts, the $\text{H}(\text{w1})\cdots\text{O}(\text{w2})$ distance is reduced from an average value of ~ 1.7 Å to ~ 1.2 Å, while the $\text{H}(\text{w1})\text{-O}(\text{w1})$ distance increases from ~ 0.96 Å to again a value of ~ 1.2 Å. When the two distances are almost equivalent, the $\text{H}(\text{w1})$ proton can be considered as shared between the two water molecules w1 and w2.

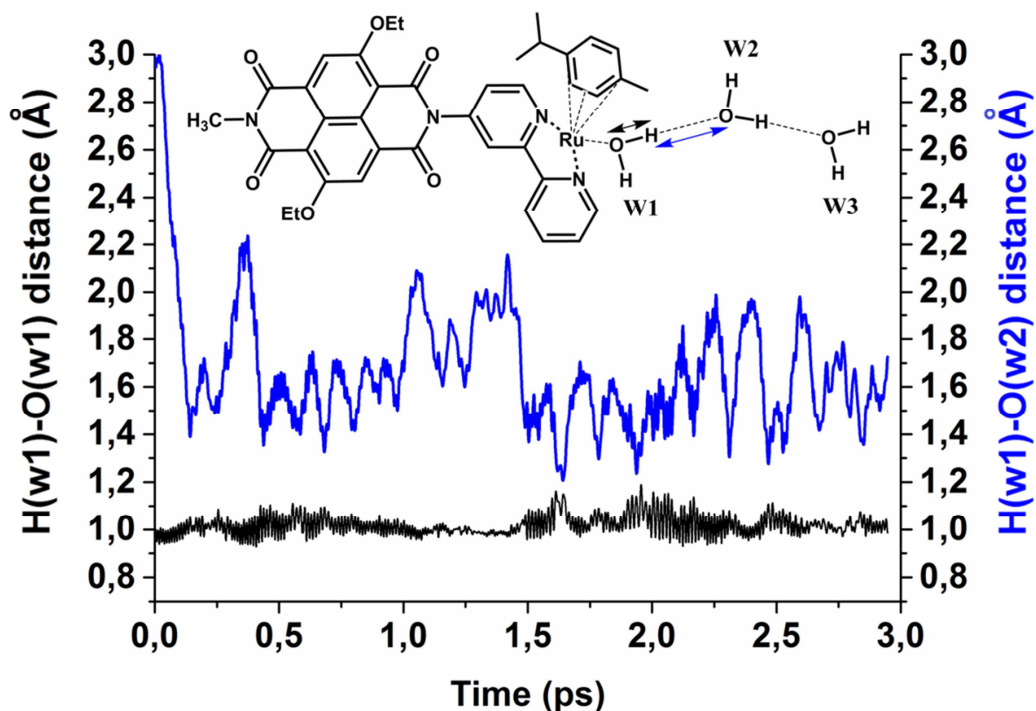
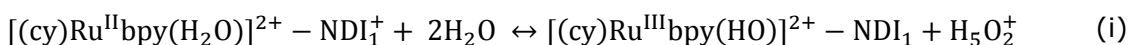


Figure 3. Time evolution of the geometrical parameters $H(w1) \cdots O(w2)$ (blue line) and $H(w1)-O(w1)$ (black line) along the unconstrained *ab initio* MD for the explicitly solvated $[(cy)Ru^{II}bpy(H_2O)]^{2+}-NDI_1^+$ complex. The inset schematically shows the dyad structure together with a few water molecules along the hydrogen bonding network.

These events represent the initial attempts of the system to spontaneously undergo the first PCET step in the water oxidation catalytic cycle and shift the redox equilibrium to the right in equation (i):



In this catalytic step, an electron is transferred from the Ru-catalyst to the NDI_1 antenna, and at the same time, a proton is released into the solvent. In equation (i) the water solvent is arbitrarily represented by only two water molecules. Given the large number of degrees of freedom involved in the solvent reorganization associated with the formation of the $[(cy)Ru^{III}bpy(HO)]^{2+} - NDI_1$ intermediate, the reaction (i) may require a time frame longer than the few ps investigated in our *ab initio* MD simulations. To accelerate the process, we perform a series of constrained MD simulations where the $H(w1) \cdots O(w2)$ distance is progressively decreased from 1.4 Å to 0.98 Å (dashed blue lines in **Figure 4**). The choice of the $H(w1) \cdots O(w2)$ distance as the reaction coordinate is justified by the observations reported for the unconstrained *ab initio* MD simulation (see **Figure 3**). At the end of the 0.98 Å simulation, an unconstrained MD trajectory is performed to test the stability of the obtained first intermediate in the catalytic cycle.

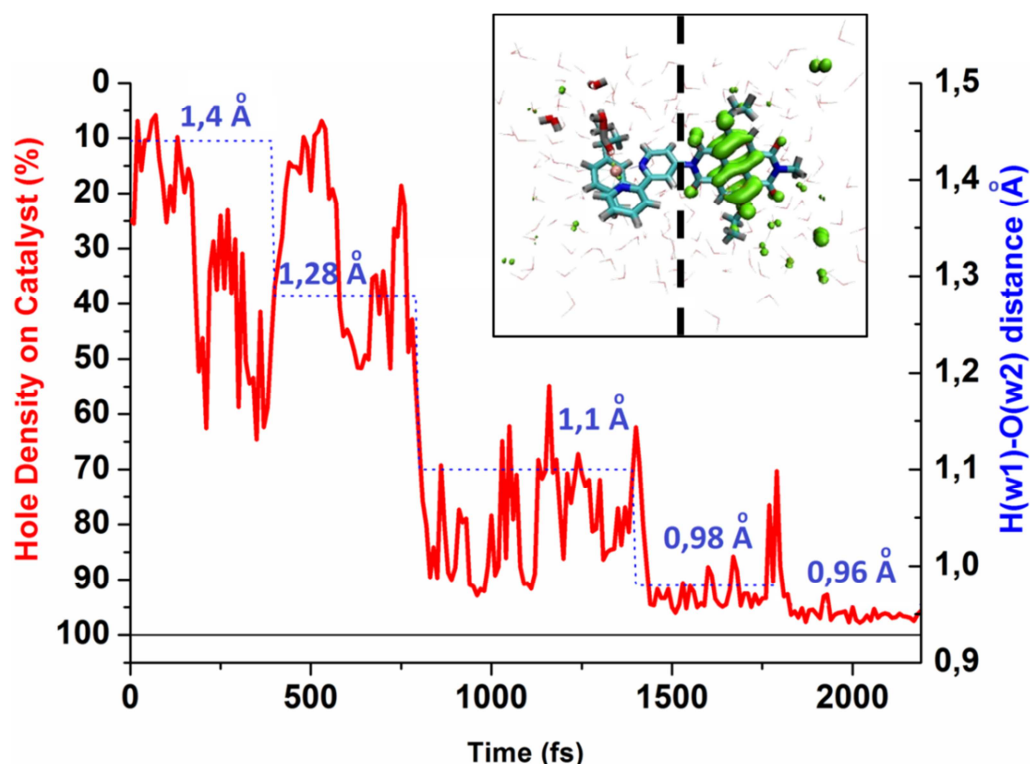


Figure 4. Red line: Percentage of the hole density obtained by integrating the spin density in the half of the simulation box including the catalyst (left hand side of the dashed black line in the inset). Blue dotted line: value of the constrained $H(w1)\cdots O(w2)$ reaction coordinate applied in the MD simulations. The results reported after 1800 fs correspond to an unconstrained simulation of the first catalytic intermediate in which the average $H(w1)-O(w2)$ distance is 0.96 Å. The inset shows a snapshot from the beginning of the trajectory corresponding to a constraint value of 1.4 Å, where the spin density is almost completely localized over the NDI_1 .

The results of the different constrained MD trajectories are collected in **Figure 4**, which shows the hole density percentage localized on the catalyst (red line). The hole density fluctuations along the trajectory provide evidence for strong coupling between the variations of the $H(w1)\cdots O(w2)$ distance and the electron transfer between NDI_1^+ and $[(cy)Ru^{II}bpy(H_2O)]^{2+}$.

For constrained distances between 1.4 Å and 1.28 Å, the hole density localized on the catalyst fluctuates around an average of ~35% of an electronic equivalent. This behaviour is observed also during the 3 ps unconstrained MD (**Figure 3**). It can be rationalized based on the similar oxidation potentials for NDI_1 and the Ru-catalyst and on the strong electronic coupling between reactant and product states. The shortening of the $H(w1)\cdots O(w2)$ distance to 1.1 Å induces a stronger localization of ~80% of the hole density on the catalyst. A further displacement of the $H(w1)$ proton towards the water molecule $w2$ reduces the charge fluctuations, leading to the $[(cy)Ru^{III}bpy(HO)]^{2+}$ catalytic

intermediate. The stability of this product state is confirmed by removing the constraint: the unconstrained MD results after 1800 fs show that the newly formed H(w1)–O(w2) bond length oscillates around an equilibrium distance of 0.96 Å. At the same time, the spin density remains localized on the catalyst, consistent with the doublet state of the Ru^{III} intermediate of the isolated catalyst, reported for comparison in **Figure SI2**. This intermediate is characterized by a spin density mostly localized on the metal center and partially on the OH ligand.

Figure 5 shows how the spin density gradually moves from the NDI₁⁺ to the Ru^{III}-catalyst along the trajectory, in response to the proton transfer. Since the ability of generalized gradient approximation (GGA) functionals to properly describe the localization of spin density has been questioned in the literature,⁸⁸ we have performed an additional test with the hybrid B3LYP functional, showing that the spin density is virtually identical to that obtained with the OPBE functional (see **Figure SI3**).

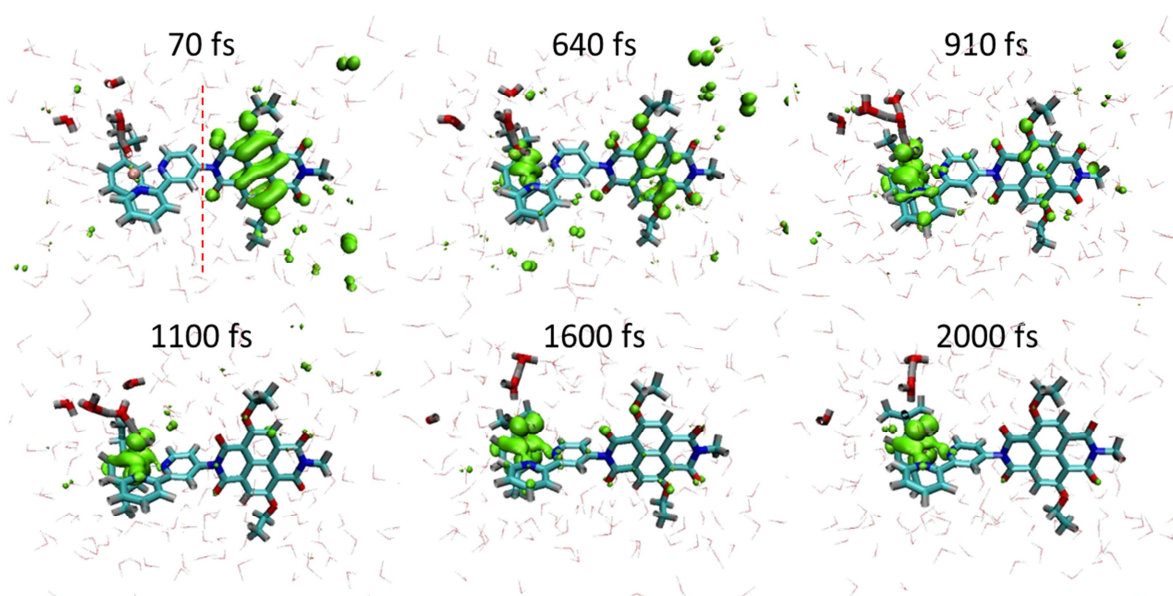


Figure 5. Spin density localization (in green) along the constrained MD trajectory shown in **Figure 4**. The labels refer to the time at which the snapshot has been taken along the collected trajectory of **Figure 4**. The spin density localized on a few water molecules is attributed to transient solvent polarization effects.

Further analysis of the constrained MD trajectories shows that the response of the solvent water molecules to the variation of the H(w1)···O(w2) distance does not only stabilize the spin density localization on the ruthenium catalyst, but also creates the conditions for the diffusion of one proton from the w1 molecule into the water bulk.

In order to characterize the proton diffusion, it is convenient to monitor how the coordination number of each oxygen atom of the solvent changes along the constrained MD trajectories. This is done by counting for each water molecule the number of protons (N_H) within a sphere centered at the oxygen position. For the analysis presented in

Figure 6, we consider a sphere of 1.2 Å radius, previously identified as the distance for which the proton can be considered as shared between the oxygen of two water molecules (see **Figure 3**). The conclusions of this analysis are not affected by a variation of $\pm 10\%$ of the sphere radius.

It is found that along the trajectory the majority of the solvent molecules retain the coordination number $N_H=2$. In **Figure 6a**, we report the oxygen coordination number of the four water molecules whose N_H value changes along the dynamical trajectory and thus play a major role in the proton diffusion. **Figure 6b** represents a snapshot extracted from the constrained MD trajectory, where these four water molecules are highlighted.

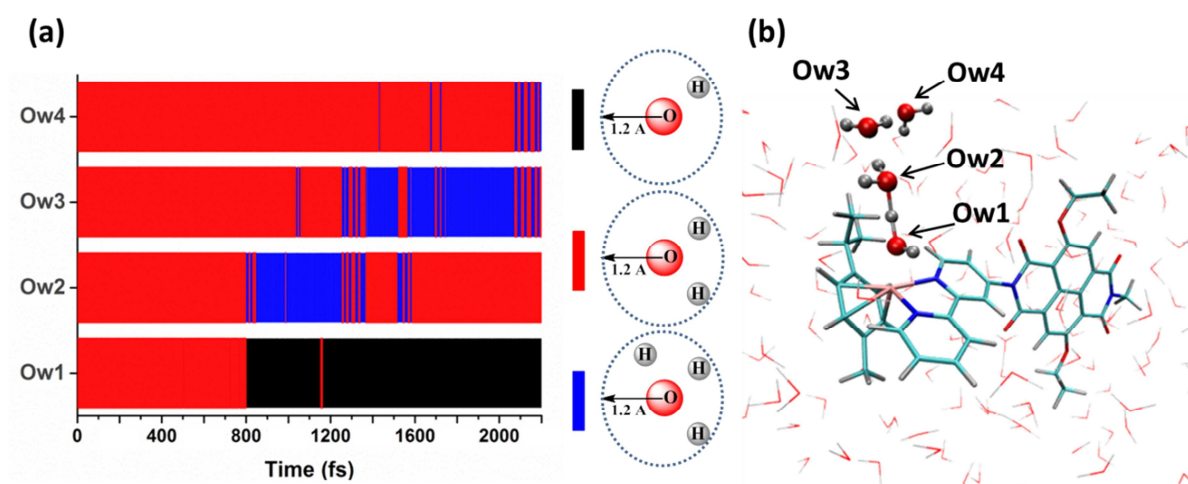


Figure 6. Path of proton diffusion from the w1 molecule into the solvent bulk along the constrained MD trajectories. (a) The color scheme corresponds to the number of protons (N_H) contained in a sphere of 1.2 Å radius centered at each oxygen atom of the solvent: $N_H=1$ (black); $N_H=2$ (red); $N_H=3$ (blue). The oxygen atoms Ow1, Ow2, Ow3, and Ow4 highlighted in (b) are the only ones for which N_H differs from 2 at any point along the trajectory. The variation of the N_H indicates that the corresponding water molecules are actively involved in the proton diffusion from w1 to w4.

From the color pattern of **Figure 6a**, it is possible to follow the path of proton diffusion from the Ru-coordinated water w1 to the bulk water molecule w4 (**Figure 6b**). Specifically, the localization of the excess proton is indicated by the blue regions associated to the oxygen coordination number $N_H=3$. It should be emphasized that while the proton jump from w1 to w2 is driven by the constraint applied to the reaction coordinate $H(w1)-O(w2)$, the subsequent proton transport steps from w2 to w3 and from w3 to w4 occur spontaneously following a Grotthuss type mechanism. The last part of the collected trajectory (Time > 1800 fs) shows that even upon removal of the constraint, the proton further diffuses throughout the solvent via the same mechanism, generating mixing entropy that decreases the probability for back reaction.

These results provide strong evidence that the reduction of the oxidized antenna and the

first catalytic water oxidation step represent a cooperative event proceeding via a concerted PCET process. The $[(\text{cy})\text{Ru}^{\text{III}}\text{bpy}(\text{HO})]^{2+}\text{-NDI}_1$ product state reached for system **1b** represents the first photoinduced catalytic intermediate in the Ru-catalyst water oxidation cycle⁴⁰. The PCET nature of this process is also in agreement with the suggested catalytic mechanism^{40,78}.

An estimate of the free energy profile along the reaction coordinate is extracted from the constrained dynamics⁷⁷. The mean force values associated with the applied constraints, together with the polynomial fit used for this analysis, are reported in **Figure SI4** in the supporting information. The obtained free energy profile for the PCET process reported in **Figure 7** shows an activation energy barrier $\Delta G^* \sim 1.7 \text{ kcal mol}^{-1}$ ($\sim 0.074 \text{ eV}$), which is equivalent to $\sim 3 k_B T$ at room temperature.

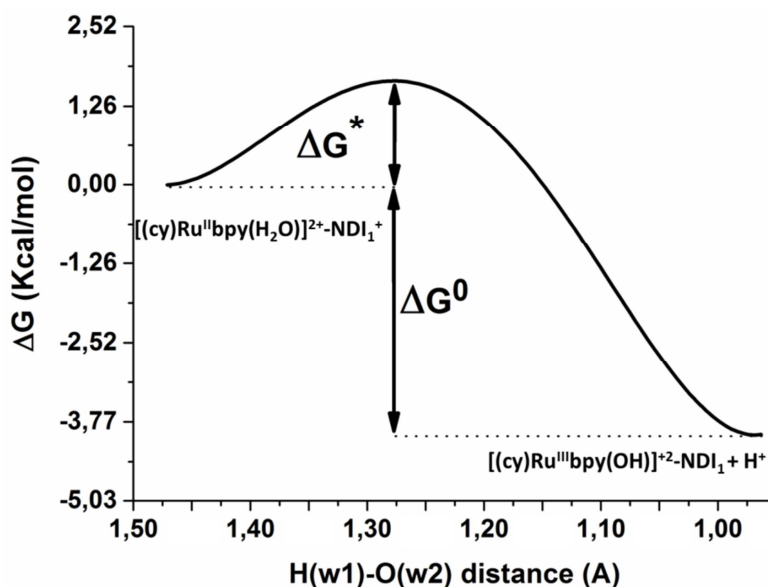


Figure 7 Free energy profile along the reaction coordinate $\text{H}(\text{w1})\text{-O}(\text{w2})$ for the first water oxidation catalytic step in system **1b**⁺. ΔG^* represents the height of the reaction energy barrier, while ΔG^0 is the reaction driving force for the transition between the initial $[(\text{cy})\text{Ru}^{\text{II}}\text{bpy}(\text{H}_2\text{O})]^{2+} - \text{NDI}_1^+$ and the final $[(\text{cy})\text{Ru}^{\text{III}}\text{bpy}(\text{OH})]^{2+} - \text{NDI}_1 + \text{H}_{\text{solvated}}^+$ state.

This low barrier suggests a very facile proton transfer step. However, from benchmark test studies for proton transfer energies,⁸⁹ it can be inferred that the barrier estimated with local density functionals of the GGA type is about 3 to 3.5 kcal mol^{-1} lower than that calculated with highly correlated *ab initio* methods. It should also be pointed out that since in our simulations the atoms are treated classically, the quantum effects associated with the proton motion are neglected. The inclusion of such effects is not expected to qualitatively change the nature of the PCET mechanism⁹⁰, but it could effectively reduce this barrier and thus increase the proton diffusion rate. A rough estimate of the zero point energy correction for the analyzed catalytic step is found to be about 3 kcal mol^{-1} ,

which is very similar to the functional related barrier underestimation. Therefore we can conclude that the functional related barrier underestimation and the quantum effects errors are in fact compensating each other to a large extent.

The reaction is found to be exothermic with the driving force $\Delta G^0 \sim -4 \text{ kcal mol}^{-1}$ ($\sim 0.17 \text{ eV}$) (see **Figure 7**). The maximum of the free energy profile corresponds to a H(w1)···O(w2) distance of 1.28 Å. Interestingly, H(w1)···O(w2) distances comparable to 1.28 Å are explored by the reactant during the unconstrained MD simulation (see **Figure 3**), although not resulting in the formation of a stable final product. Starting from the identified transition state (H(w1)···O(w2) = 1.28 Å), additional unconstrained simulations are performed with initial random velocity distributions corresponding to room temperature. Complete proton transfer between w1 and w2 (H(w1)–O(w2) < 1.1 Å) is observed several times in the same trajectory, although always followed by fast back proton transfer to w1. These results indicate that the catalytic step (i) is thermodynamically favorable. However, the reaction rate is limited by the spontaneous formation of the proton channel identified through the constrained MD simulations, which allows for a fast proton diffusion from w1 into the solvent. An accurate estimate of the kinetics of proton channel formation can be obtained through advanced sampling techniques^{91–94}, which is beyond the scope of this work.

CONCLUSIONS

This work presents a photoanode for solar water splitting involving a molecular catalyst⁶ and elucidates the dynamical details of the catalytic mechanism of the first water oxidation step. For the first time the proton and the electron dynamics is followed during the catalytic process, unambiguously showing the PCET nature of this reaction.

Semi-empirical quantum-classical simulations demonstrate that visible light photoexcitation of the NDI₁ sensitizer induces ultrafast electron injection into the TiO₂ semiconductor, activating the catalytic cycle. *Ab initio* MD simulations of the oxidized [(cy)Ru^{II}bpy(H₂O)]²⁺-NDI₁⁺ dyad (**1b**⁺) in an explicit water solvent clearly show that the electron transfer between the catalyst and the oxidized antenna is concomitant with the diffusion of one proton from the metal-coordinated water to the solvent. These simulations also underline the primary role of the solvent in providing the reaction path through the formation of a hydrogen bonding network necessary for fast proton diffusion. The entropy increase due to the proton diffusion provides further stabilization of the catalytic intermediate [(cy)Ru^{III}bpy(OH)]²⁺-NDI₁. This first catalytic step is exothermic and presents a very low activation barrier, suggesting that it can spontaneously proceed at room temperature.

The photochemical reaction simulations for our promising photoanode can be used as a

starting point for extensive DS-PEC device optimization aiming at exploring the effect of different anchoring groups,^{95–97} increasing the driving force for the subsequent steps of the catalytic water photo-oxidation cycle, reducing the charge recombination rate, and accelerating the PCET step. This can be achieved through the introduction of ancillary chromophores with complementary absorption properties and redox potentials,⁴² bridge units with rectifying properties,⁵⁹ and highly proton conductive channels.⁹⁸

ASSOCIATED CONTENT

Supporting Information. Density of states for model **1a**. Details of the AO/MO time propagation method. Comparison of spin density computed with different functionals. Spin density of first catalytic intermediate. Polynomial fit of mean force values. This material is available free of charge via the Internet at <http://pubs.acs.org>.

AUTHOR INFORMATION

Corresponding Author

*Email: f.buda@chem.leidenuniv.nl

Notes

The authors declare no competing financial interests.

ACKNOWLEDGMENTS

The use of supercomputer facilities was sponsored by NWO Physical Sciences, with financial support from the Netherlands Organization for Scientific Research (NWO). This research is financed by the NWO-ECHO project number 713.011.002.

REFERENCES

- (1) Gust, D.; Moore, T. A.; Moore, A. L. *Acc. Chem. Res.* **2009**, *42* (12), 1890–1898.
- (2) Tachibana, Y.; Vayssieres, L.; Durrant, J. R. *Nat Photon* **2012**, *6* (8), 511–518.
- (3) Dau, H.; Limberg, C.; Reier, T.; Risch, M.; Roggan, S.; Strasser, P. *ChemCatChem* **2010**, *2* (7), 724–761.
- (4) Dau, H.; Zaharieva, I. *Acc. Chem. Res.* **2009**, *42* (12), 1861–1870.
- (5) Nocera, D. G. *Acc. Chem. Res.* **2012**, *45* (5), 767–776.
- (6) Berardi, S.; Drouet, S.; Francàs, L.; Gimbert-Suriñach, C.; Guttentag, M.; Richmond, C.; Stoll, T.; Llobet, A. *Chem. Soc. Rev.* **2014**, *43* (22), 7501–7519.
- (7) Hammarström, L.; Styring, S. *Energy Environ. Sci.* **2011**, *4* (7), 2379–2388.
- (8) Yu, Z.; Li, F.; Sun, L. *Energy Environ. Sci.* **2015**, *8* (3), 760–775.
- (9) Young, K. J.; Martini, L. A.; Milot, R. L.; Snoeberger III, R. C.; Batista, V. S.; Schmuttenmaer, C. A.; Crabtree, R. H.; Brudvig, G. W. *Coordination Chemistry Reviews* **2012**, *256* (21–22), 2503–2520.
- (10) Hamann, T. W. *Nat Mater* **2014**, *13* (1), 3–4.
- (11) Scholes, G. D.; Fleming, G. R.; Olaya-Castro, A.; van Grondelle, R. *Nat Chem* **2011**, *3* (10), 763–774.

- (12) Tran, P. D.; Wong, L. H.; Barber, J.; Loo, J. S. C. *Energy Environ. Sci.* **2012**, 5 (3), 5902–5918.
- (13) Fujishima, A.; Honda, K. *Nature* **1972**, 238 (5358), 37–38.
- (14) Youngblood, W. J.; Lee, S.-H. A.; Kobayashi, Y.; Hernandez-Pagan, E. A.; Hoertz, P. G.; Moore, T. A.; Moore, A. L.; Gust, D.; Mallouk, T. E. *J. Am. Chem. Soc.* **2009**, 131 (3), 926–927.
- (15) Ashford, D. L.; Gish, M. K.; Vannucci, A. K.; Brennaman, M. K.; Templeton, J. L.; Papanikolas, J. M.; Meyer, T. J. *Chem. Rev.* **2015**, 115 (23), 13006–13049.
- (16) Zhao, Y.; Swierk, J. R.; Megiatto, J. D.; Sherman, B.; Youngblood, W. J.; Qin, D.; Lentz, D. M.; Moore, A. L.; Moore, T. A.; Gust, D.; Mallouk, T. E. *PNAS* **2012**, 109 (39), 15612–15616.
- (17) Maeda, K.; Teramura, K.; Lu, D.; Takata, T.; Saito, N.; Inoue, Y.; Domen, K. *Nature* **2006**, 440 (7082), 295–295.
- (18) Brillet, J.; Yum, J.-H.; Cornuz, M.; Hisatomi, T.; Solaraska, R.; Augustynski, J.; Graetzel, M.; Sivula, K. *Nat Photon* **2012**, 6 (12), 824–828.
- (19) Reece, S. Y.; Hamel, J. A.; Sung, K.; Jarvi, T. D.; Esswein, A. J.; Pijpers, J. J. H.; Nocera, D. G. *Science* **2011**, 334 (6056), 645–648.
- (20) Higashi, M.; Domen, K.; Abe, R. *J. Am. Chem. Soc.* **2012**, 134 (16), 6968–6971.
- (21) Yang, J.; Wang, D.; Han, H.; Li, C. *Acc. Chem. Res.* **2013**, 46 (8), 1900–1909.
- (22) Zhang, J.; Wang, X. *Angew. Chem. Int. Ed.* **2015**, 54 (25), 7230–7232.
- (23) Blakemore, J. D.; Gray, H. B.; Winkler, J. R.; Müller, A. M. *ACS Catal.* **2013**, 3 (11), 2497–2500.
- (24) Ronconi, F.; Syrgiannis, Z.; Bonasera, A.; Prato, M.; Argazzi, R.; Caramori, S.; Cristino, V.; Bignozzi, C. A. *J. Am. Chem. Soc.* **2015**, 137 (14), 4630–4633.
- (25) Klepser, B. M.; Bartlett, B. M. *J. Am. Chem. Soc.* **2014**, 136 (5), 1694–1697.
- (26) Gao, Y.; Ding, X.; Liu, J.; Wang, L.; Lu, Z.; Li, L.; Sun, L. *J. Am. Chem. Soc.* **2013**, 135 (11), 4219–4222.
- (27) Duan, L.; Bozoglian, F.; Mandal, S.; Stewart, B.; Privalov, T.; Llobet, A.; Sun, L. *Nat Chem* **2012**, 4 (5), 418–423.
- (28) Kärkäs, M. D.; Verho, O.; Johnston, E. V.; Åkermark, B. *Chem. Rev.* **2014**, 114 (24), 11863–12001.
- (29) Swierk, J. R.; McCool, N. S.; Mallouk, T. E. *J. Phys. Chem. C* **2015**.
- (30) Ding, X.; Gao, Y.; Zhang, L.; Yu, Z.; Liu, J.; Sun, L. *ACS Catal.* **2014**, 4 (7), 2347–2350.
- (31) Li, H.; Li, F.; Zhang, B.; Zhou, X.; Yu, F.; Sun, L. *J. Am. Chem. Soc.* **2015**, 137 (13), 4332–4335.
- (32) Moore, G. F.; Blakemore, J. D.; Milot, R. L.; Hull, J. F.; Song, H.; Cai, L.; Schmuttenmaer, C. A.; Crabtree, R. H.; Brudvig, G. W. *Energy Environ. Sci.* **2011**, 4 (7), 2389–2392.
- (33) Pastore, M.; De Angelis, F. *J. Am. Chem. Soc.* **2015**, 137 (17), 5798–5809.
- (34) Vagnini, M. T.; Smeigh, A. L.; Blakemore, J. D.; Eaton, S. W.; Schley, N. D.; D’Souza, F.; Crabtree, R. H.; Brudvig, G. W.; Co, D. T.; Wasielewski, M. R. *PNAS* **2012**, 109 (39), 15651–15656.
- (35) Ji, Z.; He, M.; Huang, Z.; Ozkan, U.; Wu, Y. *J. Am. Chem. Soc.* **2013**, 135 (32), 11696–11699.
- (36) Norris, M. R.; Concepcion, J. J.; Fang, Z.; Templeton, J. L.; Meyer, T. J. *Angew. Chem. Int. Ed.* **2013**, 52 (51), 13580–13583.
- (37) Ai, X.; Anderson, N. A.; Guo, J.; Lian, T. *J. Phys. Chem. B* **2005**, 109 (15), 7088–7094.

- (38) Pastore, M.; Selloni, A.; Fantacci, S.; Angelis, F. D. In *First Principles Approaches to Spectroscopic Properties of Complex Materials*; Valentin, C. D., Botti, S., Cococcioni, M., Eds.; Topics in Current Chemistry; Springer Berlin Heidelberg, 2014; pp 1–45.
- (39) Chen, J.; Li, Y.-F.; Sit, P.; Selloni, A. *J. Am. Chem. Soc.* **2013**, *135* (50), 18774–18777.
- (40) Vallés-Pardo, J. L.; Guijt, M. C.; Iannuzzi, M.; Joya, K. S.; de Groot, H. J. M.; Buda, F. *ChemPhysChem* **2012**, *13* (1), 140–146.
- (41) de Respinis, M.; Joya, K. S.; De Groot, H. J. M.; D’Souza, F.; Smith, W. A.; van de Krol, R.; Dam, B. *J. Phys. Chem. C* **2015**, *119* (13), 7275–7281.
- (42) Monti, A.; de Groot, H. J. M.; Buda, F. *J. Phys. Chem. C* **2014**, *118* (29), 15600–15609.
- (43) Sakai, N.; Mareda, J.; Vauthey, E.; Matile, S. *Chem. Commun.* **2010**, 46 (24), 4225–4237.
- (44) Kishore, R. S. K.; Kel, O.; Banerji, N.; Emery, D.; Bollot, G.; Mareda, J.; Gomez-Casado, A.; Jonkheijm, P.; Huskens, J.; Maroni, P.; Borkovec, M.; Vauthey, E.; Sakai, N.; Matile, S. *J. Am. Chem. Soc.* **2009**, *131* (31), 11106–11116.
- (45) Yushchenko, O.; Villamaina, D.; Sakai, N.; Matile, S.; Vauthey, E. *J. Phys. Chem. C* **2015**, *119* (27), 14999–15008.
- (46) Sakai, N.; Bhosale, R.; Emery, D.; Mareda, J.; Matile, S. *J. Am. Chem. Soc.* **2010**, *132* (20), 6923–6925.
- (47) Avinash, M. B.; Swathi, K.; Narayan, K. S.; Govindaraju, T. *ACS Appl. Mater. Interfaces* **2016**.
- (48) Schroot, R.; Schlotthauer, T.; Schubert, U. S.; Jäger, M. *Macromolecules* **2016**, *49* (6), 2112–2123.
- (49) Bosma, W. B.; Fried, L. E.; Mukamel, S. *The Journal of Chemical Physics* **1993**, *98* (6), 4413–4421.
- (50) Auer, B.; Soudackov, A. V.; Hammes-Schiffer, S. *J. Phys. Chem. B* **2012**, *116* (26), 7695–7708.
- (51) Eisenmayer, T. J.; Buda, F. *ChemPhysChem* **2014**, *15* (15), 3258–3263.
- (52) Jackson, M. N.; Surendranath, Y. *J. Am. Chem. Soc.* **2016**, *138* (9), 3228–3234.
- (53) ADF: The ADF program for accurate density functional theory calculations of molecules <http://www.scm.com/ADF/> (accessed Mar 7, 2013).
- (54) te Velde, G.; Bickelhaupt, F. M.; Baerends, E. J.; Fonseca Guerra, C.; van Gisbergen, S. J. A.; Snijders, J. G.; Ziegler, T. *Journal of Computational Chemistry* **2001**, *22* (9), 931–967.
- (55) Swart, M.; Ehlers, A. W.; Lammertsma *, K. *Molecular Physics* **2004**, *102* (23-24), 2467–2474.
- (56) Hoffmann, R. *The Journal of Chemical Physics* **1963**, *39* (6), 1397–1412.
- (57) Ammeter, J. H.; Bürgi, H. B.; Thibeault, J. C.; Hoffmann, R. *J. Am. Chem. Soc.* **1978**, *100* (12), 3686–3692.
- (58) Alvarez, S. *Table of parameters for Extended Hückel Calculations* **1995**, Universitat de Barcelona.
- (59) Monti, A.; Negre, C. F. A.; Batista, V. S.; Rego, L. G. C.; de Groot, H. J. M.; Buda, F. *J. Phys. Chem. Lett.* **2015**, *6* (12), 2393–2398.
- (60) Hoff, D. A.; Silva, R.; Rego, L. G. C. *J. Phys. Chem. C* **2011**, *115* (31), 15617–15626.
- (61) da Silva, R.; Hoff, D. A.; Rego, L. G. C. *Journal of Physics: Condensed Matter* **2015**, *27* (13), 134206.
- (62) Hoff, D. A.; da Silva, R.; Rego, L. G. C. *J. Phys. Chem. C* **2012**, *116* (40), 21169–21178.
- (63) Abuabara, S. G.; Rego, L. G. C.; Batista, V. S. *J. Am. Chem. Soc.* **2005**, *127* (51), 18234–18242.

- (64) Rego, L. G. C.; Hames, B. C.; Mazon, K. T.; Joswig, J.-O. *J. Phys. Chem. C* **2014**, *118* (1), 126–134.
- (65) CPMD, <http://www.cpmd.org/>, Copyright IBM Corp 1990-2008, Copyright MPI für Festkörperforschung Stuttgart 1997-2001.
- (66) Lin, I.-C.; Coutinho-Neto, M. D.; Felsenheimer, C.; von Lilienfeld, O. A.; Tavernelli, I.; Rothlisberger, U. *Phys. Rev. B* **2007**, *75* (20), 205131.
- (67) Troullier, N.; Martins, J. L. *Phys. Rev. B* **1991**, *43* (3), 1993–2006.
- (68) Klamt, A.; Jonas, V. *The Journal of Chemical Physics* **1996**, *105* (22), 9972–9981.
- (69) Klamt, A. *J. Phys. Chem.* **1995**, *99* (7), 2224–2235.
- (70) Carvalho, A. T. P.; Swart, M. *J. Chem. Inf. Model.* **2014**, *54* (2), 613–620.
- (71) Groenhof, A. R.; Ehlers, A. W.; Lammertsma, K. *J. Am. Chem. Soc.* **2007**, *129* (19), 6204–6209.
- (72) Conradie, J.; Ghosh, A. *J. Chem. Theory Comput.* **2007**, *3* (3), 689–702.
- (73) Stephens, P. J.; Devlin, F. J.; Chabalowski, C. F.; Frisch, M. J. *J. Phys. Chem.* **1994**, *98* (45), 11623–11627.
- (74) Ma, C.; Piccinin, S.; Fabris, S. *ACS Catal.* **2012**, *2* (7), 1500–1506.
- (75) Otter, W. K. den; Briels, W. J. *The Journal of Chemical Physics* **1998**, *109* (11), 4139–4146.
- (76) Sprik, M.; Ciccotti, G. *The Journal of Chemical Physics* **1998**, *109* (18), 7737–7744.
- (77) Ciccotti, G.; Ferrario, M. *Molecular Simulation* **2004**, *30* (11-1), 787–793.
- (78) Joya, K. S.; Vallés-Pardo, J. L.; Joya, Y. F.; Eisenmayer, T.; Thomas, B.; Buda, F.; de Groot, H. J. M. *ChemPlusChem* **2013**, *78* (1), 35–47.
- (79) Kanan, M. W.; Nocera, D. G. *Science* **2008**, *321* (5892), 1072–1075.
- (80) Maggio, E.; Martsinovich, N.; Troisi, A. *Angew. Chem. Int. Ed.* **2013**, *52* (3), 973–975.
- (81) Ding, W.; Negre, C. F. A.; Vogt, L.; Batista, V. S. *J. Chem. Theory Comput.* **2014**, *10* (8), 3393–3400.
- (82) Hassanali, A.; Giberti, F.; Cuny, J.; Kühne, T. D.; Parrinello, M. *PNAS* **2013**, *110* (34), 13723–13728.
- (83) Marx, D.; Chandra, A.; Tuckerman, M. E. *Chem. Rev.* **2010**, *110* (4), 2174–2216.
- (84) Agmon, N. *Chemical Physics Letters* **1995**, *244* (5–6), 456–462.
- (85) Codorniu-Hernández, E.; Kusalik, P. G. *PNAS* **2013**, *110* (34), 13697–13698.
- (86) Liang, R.; Li, H.; Swanson, J. M. J.; Voth, G. A. *PNAS* **2014**, *111* (26), 9396–9401.
- (87) de Grotthuss, C. J. T. *Biochimica et Biophysica Acta (BBA) - Bioenergetics* **2006**, *1757* (8), 871–875.
- (88) Cheng, J.; Sulpizi, M.; VandeVondele, J.; Sprik, M. *ChemCatChem* **2012**, *4* (5), 636–640.
- (89) Nachimuthu, S.; Gao, J.; Truhlar, D. G. *Chemical Physics* **2012**, *400*, 8–12.
- (90) Tuckerman, M. E.; Marx, D.; Klein, M. L.; Parrinello, M. *Science* **1997**, *275* (5301), 817–820.
- (91) Pietrucci, F.; Saitta, A. M. *Proc. Natl. Acad. Sci. U.S.A.* **2015**, *112* (49), 15030–15035.
- (92) Bolhuis, P. G.; Chandler, D.; Dellago, C.; Geissler, P. L. *Annual Review of Physical Chemistry* **2002**, *53* (1), 291–318.
- (93) Laio, A.; Parrinello, M. *PNAS* **2002**, *99* (20), 12562–12566.
- (94) Geissler, P. L.; Dellago, C.; Chandler, D.; Hutter, J.; Parrinello, M. *Science* **2001**, *291* (5511), 2121–2124.
- (95) Mathew, S.; Yella, A.; Gao, P.; Humphry-Baker, R.; Curchod, B. F. E.; Ashari-Astani, N.; Tavernelli, I.; Rothlisberger, U.; Nazeeruddin, M. K.; Grätzel, M. *Nat Chem* **2014**, *6* (3), 242–247.
- (96) Ambrosio, F.; Martsinovich, N.; Troisi, A. *J. Phys. Chem. Lett.* **2012**, *3* (11), 1531–1535.

- (97) Zhang, L.; Cole, J. M. *ACS Applied Materials & Interfaces* **2015**, 7, 3427–3455.
- (98) Matsuki, Y.; Iwamoto, M.; Mita, K.; Shigemi, K.; Matsunaga, S.; Oiki, S. *J. Am. Chem. Soc.* **2016**.

Table of Contents and Abstract Graphics

